# Exciton Transport in a Germanium Quantum Dot Ladder

Hsiao, T. K.; Cova Fariña, P.; Oosterhout, S. D.; Jirovec, D.; Zhang, X.; Van Diepen, C. J.; Lawrie, W. I.L.; Wang, C. A.; Sammak, A.; Scappucci, G.

**DOI**
10.1103/PhysRevX.14.011048

**Publication date**
2024

**Document Version**
Final published version

**Published in**
Physical Review X

**Citation (APA)**
Hsiao, T. K., Cova Fariña, P., Oosterhout, S. D., Jirovec, D., Zhang, X., Van Diepen, C. J., Lawrie, W. I. L., Wang, C. A., Sammak, A., Scappucci, G., Veldhorst, M., & Vandersypen, L. M. K. (2024). Exciton Transport in a Germanium Quantum Dot Ladder. *Physical Review X*, *14*(1), Article 011048. https://doi.org/10.1103/PhysRevX.14.011048

# Exciton Transport in a Germanium Quantum Dot Ladder

T.-K. Hsiao,[1,*,†] P. Cova Fariña,[1,*] S. D. Oosterhout,[1,2] D. Jirovec,[1] X. Zhang,[1] C. J. van Diepen,[1,‡] W. I. L. Lawrie,[1,‡] C.-A. Wang,[1] A. Sammak,[1,2] G. Scappucci,[1] M. Veldhorst,[1] E. Demler,[3] and L. M. K. Vandersypen[1,§]

[1]*QuTech and Kavli Institute of Nanoscience, Delft University of Technology, 2600 GA Delft, The Netherlands*
[2]*Netherlands Organisation for Applied Scientific Research (TNO), 2628 CK Delft, The Netherlands*
[3]*Institute for Theoretical Physics, Wolfgang-Pauli-Straße 27, ETH Zurich, 8093 Zurich, Switzerland*

(Received 5 July 2023; revised 8 December 2023; accepted 5 February 2024; published 14 March 2024)

Quantum systems with engineered Hamiltonians can be used to study many-body physics problems to provide insights beyond the capabilities of classical computers. Semiconductor gate-defined quantum dot arrays have emerged as a versatile platform for realizing generalized Fermi-Hubbard physics, one of the richest playgrounds in condensed matter physics. In this work, we employ a germanium $4 \times 2$ quantum dot array and show that the naturally occurring long-range Coulomb interaction can lead to exciton formation and transport. We tune the quantum dot ladder into two capacitively coupled channels and exploit Coulomb drag to probe the binding of electrons and holes. Specifically, we shuttle an electron through one leg of the ladder and observe that a hole is dragged along in the second leg under the right conditions. This corresponds to a transition from single-electron transport in one leg to exciton transport along the ladder. Our work paves the way for the study of excitonic states of matter in quantum dot arrays.

DOI: 10.1103/PhysRevX.14.011048

Subject Areas: Condensed Matter Physics, Quantum Physics, Quantum Information, Semiconductor Physics

## I. INTRODUCTION

Quantum systems with well-controlled interaction parameters can shed light on the physics of strongly correlated many-body quantum systems [1,2]. Electrostatically defined semiconductor quantum dot arrays, owing to their *in situ* tunability of electrochemical potentials and relevant energy scales which can far exceed the thermal energy, have become an attractive platform for studying a wide variety of fermionic systems [3–6]. Over the past few years, the techniques for control and probing of quantum dot simulators has progressed significantly. This platform and closely related donor arrays have been used as a small-scale simulator of Mott-Hubbard physics [7–9], Nagaoka ferromagnetism [10], Heisenberg antiferromagnetic spin chains [11], resonating valence bond states [12], and the Su-Schrieffer-Heeger model [13].

The charge carriers confined in quantum dot arrays exhibit an intrinsic long-range Coulomb interaction which is essential for a wide range of interesting phenomena. The long-range interaction induces spontaneous ordering of charges in a flat potential landscape to form a Wigner crystal [14,15]. Similar spontaneous charge ordering occurs in lattice potentials that are fractionally filled [16,17]. Also, pair density wave states crucially rely on nonlocal interactions [18]. When particles of opposite charge are involved, the long-range Coulomb interaction is attractive instead of repulsive, and composite particles can be formed. The attractive interaction between electrons and holes is the essential ingredient for exciton formation [19], excitonic insulators [20], and exciton condensates [21]. In lattices that are close to fractional filling, a charge-transfer exciton can bind one or two holes, giving rise to a polariton or trimer [22]. It has been suggested that this trimer can give rise to unconventional superconductivity [23].

The long-range Coulomb interaction combined with the precise control of the lattice filling, interdot charge tunneling, and the spin degree of freedom thus allow quantum dot systems access to a wealth of interesting many-body phenomena in Coulomb-mediated states of matters. In ultracold

*These authors contributed equally to this work.
†Present address: Department of Physics, National Tsing Hua University, Hsinchu 30013, Taiwan.
‡Present address: Niels Bohr Institute, University of Copenhagen, Copenhagen, Denmark.
§L.M.K.Vandersypen@tudelft.nl

atoms systems, combining tunneling with long-range interactions has only recently been achieved [24,25], and remains challenging. For ultracold atoms in optical lattices, the Hamiltonian is usually limited to on-site interactions and tunneling [26,27]. Conversely, for atoms with a large magnetic moment or dipolar molecules in optical lattices, long-range dipolar interactions exist, but tunneling is generally absent [28,29]. In such platforms as well as for Rydberg atoms trapped by optical tweezers, the focus has therefore been on studying various spin models [30–32].

In low-dimensional solid-state systems, a clear manifestation of long-range Coulomb interactions is Coulomb drag. In a two-channel system, a current imposed by a voltage bias across one channel (the drive channel) leads to a current or voltage across a second channel (the drag channel) [33]. Coulomb drag can take two forms. "Positive" Coulomb drag occurs when an electron in the drive channel pushes electrons in the drag channel forward due to Coulomb-mediated momentum transfer [34]. "Negative" Coulomb drag can result from Wigner-crystal physics [35] or from exciton formation [33,36], in which the motion of a charge carrier in the drive channel pulls along a charge carrier of opposite sign in the drag channel. The negative Coulomb drag effect from exciton formation has been observed in double quantum wells in the quantum Hall regime [33,37,38], double quantum wires [39], and 2D materials [40–42]. In these works, the negative Coulomb drag is interpreted as resulting from interchannel exciton transport. Whereas Coulomb drag can arise from interactions between classical charges, in the quantum dot platform, the motion of charges and excitons occurs by tunneling and cotunneling, respectively, which are intrinsically quantum mechanical processes. Coulomb drag then serves as a precursor for exciton condensation and excitonic insulator phases.

Excitonic states can be described theoretically using a two-channel Hubbard model with $N \times 2$ sites [43–45],

$$H = -t\sum_{\langle i,j\rangle,\sigma} c^{\dagger}_{i\sigma}c_{j\sigma} + U\sum_{i}\frac{n_i(n_i-1)}{2} + U'\sum_{\langle i,j\rangle} n_i n_j + V\sum_{i\in\alpha,j\in\beta} n_i n_j + V'\sum_{i\in\alpha,j\in\beta} n_i n_j, \quad (1)$$

where $c_{i\sigma}$ denotes the annihilation operator of a spin-1/2 fermion with spin $\sigma\in\{\uparrow,\downarrow\}$ at site $i$ of a two-channel system where sites 1 to $N$ are located in channel $\alpha$ and sites $(N+1)$ to $2N$ are part of channel $\beta$, and $\langle i,j\rangle$ sums over neighboring sites in the same channel. The number operator is given by $n_i = c^{\dagger}_{i\uparrow}c_{i\uparrow} + c^{\dagger}_{i\downarrow}c_{i\downarrow}$, $t$ is the tunnel coupling within the same channel, $U$ the on-site Coulomb interaction, $U'$ is the nearest-neighbor Coulomb interaction within the same channel, $V$ is the nearest-neighbor interchannel Coulomb interaction, and $V'$ is the diagonal interchannel Coulomb interaction. When the two channels are occupied by charge carriers of opposite sign, the interchannel interactions are attractive. Note that we consider systems without hopping between the two channels, and interaction terms beyond nearest-neighbor or diagonal sites are neglected. Furthermore, in Eq. (1) we assume homogeneous tunnel couplings and Coulomb interactions. To describe systems with inhomogeneous couplings, we will use $t_{ij}$ and $V_{ij}$ to denote the tunnel coupling and interchannel Coulomb interaction between site $i$ and $j$.

This model can describe the conduction band and valence band in a material, and also two capacitively coupled channels. Earlier works have reported on arrays of metallic or superconducting tunnel junctions [46–48] and small quantum dot arrays [49]. However, these systems lack the control knobs for individual interaction parameters and the probes for the quantum state at each site. In comparison, when an $N \times 2$ quantum dot ladder is tuned to host electrons in one channel and holes in the other channel, thanks to the advanced control and probing capabilities, it can be used as a versatile platform for studying excitonic physics.

Many years of work on quantum dot systems have led to steady scaling of linear arrays [50–52]. Furthermore, several reports on two-dimensional quantum dot arrays have appeared using GaAs [10,53], silicon [54,55], and germanium [56] as the host material. Among the various host materials, germanium is particularly promising to scale to large arrays thanks to the low disorder and light effective mass [57,58]. Even a $4 \times 4$ Ge quantum dot array has been realized [59], albeit with shared controlled electrochemical potentials and tunnel couplings.

In this work we use a $4 \times 2$ Ge quantum dot ladder as an excitonic system, doubling the size of fully controlled Ge quantum dot arrays [56]. We activate hopping along the legs of the ladder but suppress hopping between the legs. In this way, two capacitively coupled channels of quantum dots are formed. The charge carriers in this platform are holes arising from the valence band. A missing hole on top of a singly occupied background of holes effectively defines an electron. We control the electrochemical potentials of the array such that the top channel hosts an electron and the bottom channel can host a hole. To explore the formation of excitons, we use real-time charge sensing to study under what conditions the imposed motion of an electron through the top channel drags along a hole in the bottom channel through the long-range Coulomb interaction.

## II. DEVICE AND EXPERIMENTAL APPROACH

The experiment is carried out in an electrostatically defined $4 \times 2$ hole quantum dot array, which is fabricated in a Ge/SiGe quantum well heterostructure [60]. Figure 1(a) shows a device image, with the positions of the dots and charge sensors as indicated by the labeled circles. Figure 1(b) shows a schematic gate stack of the device. Screening gates, plunger gates, and barrier gates were fabricated in successive lithography steps (see the

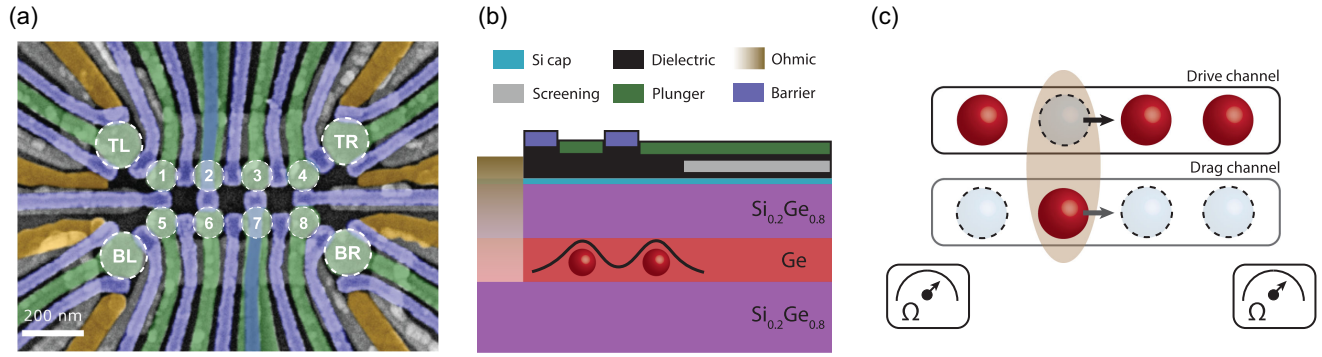


FIG. 1. (a) A false-color scanning electron microscope image of a device nominally identical to the one used in this work. The dashed white circles indicate the intended positions of the $4 \times 2$ dot array and sensing dots. (b) Schematic cross section of the gate stack and a germanium quantum well heterostructure. Holes are confined in the 55-nm-deep quantum well. Gate layers with different functions are drawn in colors shown in the legend. (c) Schematics illustrating the Coulomb drag of a hole in the bottom channel by the (imposed) motion of an electron (missing hole) in the top channel of a $4 \times 2$ quantum dot array. The bound state of an electron and hole (an exciton) arises from the interchannel Coulomb interaction. Two charge sensors, located at the bottom left and bottom right corners, are used to probe the charge configuration of the array.

Appendix for details), using a device design that can be easily extended to longer bilinear quantum dot ladders. We refer to the path from dot 1 to dot 4 as the top channel (drive channel) and to the path from dot 5 to dot 8 as the bottom channel (drag channel). Quantum dots are formed by applying negative dc voltages on a set of plunger gates $P$ and barrier gates $B$, to accumulate and confine holes in the quantum well in the area between the screening gates. The charge occupation of the $4 \times 2$ array is denoted $\left(\begin{smallmatrix} O_1 & O_2 & O_3 & O_4 \\ O_5 & O_6 & O_7 & O_8 \end{smallmatrix}\right)$, where $O_i$ represents the number of holes in dot $i$. The structure allows for individual control of all ten nearest-neighbor tunnel couplings. Plunger gates and barrier gates are additionally connected to high-frequency lines via bias tees to allow fast control of electrochemical potentials and tunnel couplings.

In this experiment the plunger and barrier gates are virtualized such that changing a virtual plunger $P_i'$ independently controls the electrochemical potential $\epsilon_i$ of dot $i$, and changing a virtual barrier $B_{ij}'$ mainly modulates the tunnel coupling $t_{ij}$ between neighboring dots $i$ and $j$ without influencing the dot potentials. In this device four charge sensors [bottom left (BL), bottom right (BR), top left (TR) and top right (TR)] can be formed at the four corners of the array. They serve both as detectors for the charge occupation and as reservoirs. In this experiment we use only the BL and BR sensors for charge sensing, with multiplexed rf reflectometry (TL and TR are used as reservoirs). The plunger gates for the BL and BR sensors are also included in the gate virtualization, such that sweeping a plunger gate in the array does not shift the sensor peak position. Therefore, the sensors are mostly sensitive to changes of the charge occupation in the array. While jumps in the charge sensor peak position could in principle affect the loading fidelity, the Coulomb peaks are broad enough such that this effect is negligible for the experiments described below. Thus, we can simultaneously use them as charge sensors and reservoirs without a measurable impact in loading fidelity.

To study exciton formation via the Coulomb drag effect, we will aim to initialize the device in the $\left(\begin{smallmatrix} 1 & 1 & 1 & 1 \\ 0 & 0 & 0 & 0 \end{smallmatrix}\right)$ charge state, where each top-channel dot is occupied by one hole and the bottom channel is empty. Because the charge carriers in the array are holes originating from the valence band, removing a hole in the top channel amounts to adding an electron relative to the singly filled background of holes (see Fig. 2). We can thus load an electron to the top channel by emptying a dot [e.g., pulsing to the (0111) charge state in the top channel]. The electrochemical potentials of the bottom dots in the $\left(\begin{smallmatrix} 1 & 1 & 1 & 1 \\ 0 & 0 & 0 & 0 \end{smallmatrix}\right)$ configuration are aligned with each other, such that loading a hole from the reservoir to the bottom channel costs the same energy regardless of its position. We label this energy cost $E$ (Fig. 2). When $E$ is lower than the nearest-neighbor interchannel Coulomb interaction $V_{ij}$, a hole will be attracted in the bottom channel by the top-channel electron, reaching, e.g., the charge state $\left(\begin{smallmatrix} 0 & 1 & 1 & 1 \\ 1 & 0 & 0 & 0 \end{smallmatrix}\right)$. An electron-hole pair is thus formed bound by $V_{ij}$, which constitutes an interchannel exciton (strictly speaking, $V_{ij}$ must here be corrected by intrachannel and diagonal Coulomb interactions; we will neglect these corrections to simplify the discussion but they are included when aligning the bottom dot potentials). Furthermore, if the system Hamiltonian favors an exciton ground state, pushing the electron (the missing hole) through the top channel will cause the hole in the bottom to move together with the electron [Figs. 1(c) and 2].

## III. QUANTUM DOT LADDER FORMATION AND TUNE-UP

Figure 3(a) shows charge stability diagrams for the interchannel dot pair 1-5 near the $\left(\begin{smallmatrix} 1 & 1 & 1 & 1 \\ 0 & 0 & 0 & 0 \end{smallmatrix}\right)$ charge

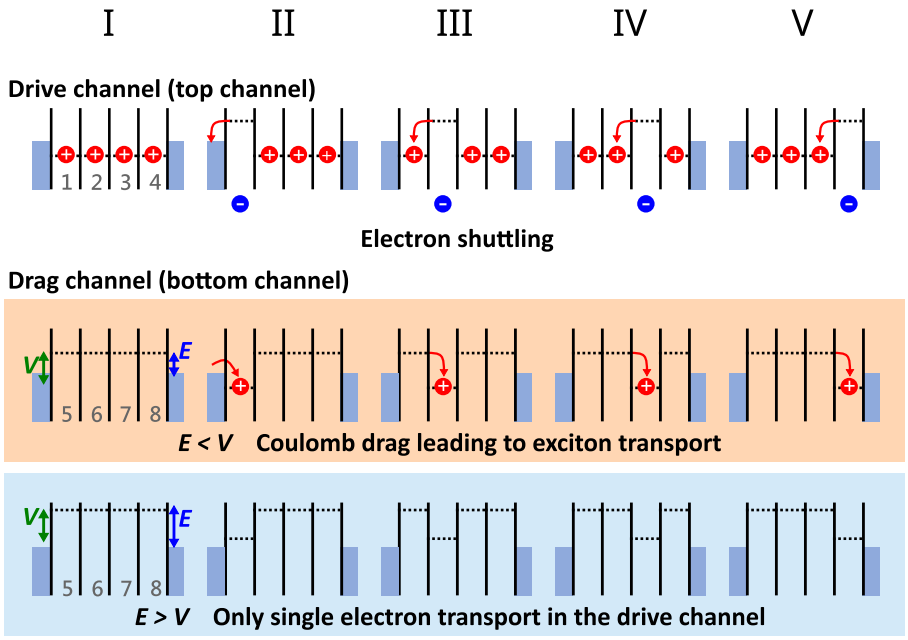


FIG. 2. Schematics illustrating the experimental scheme for probing exciton formation through Coulomb drag. The first row shows the ladder diagrams of the drive channel. The vertical axis is an energy axis, the horizontal axis is space. Vertical black lines indicate tunnel barriers, the blue shaded region represents the reservoir, which is filled up to the Fermi level. Phase I: Each dot is filled with one hole and the dot potentials are aligned. Phase II: The leftmost hole is pushed out by raising $\epsilon_1$, which can be viewed as loading an electron in dot 1. Phase III: $\epsilon_1$ is lowered and $\epsilon_2$ is raised. The electron moves to dot 2. Phase IV: $\epsilon_2$ is lowered and $\epsilon_3$ is raised. The electron moves to dot 3. Phase V: $\epsilon_3$ is lowered and $\epsilon_4$ is raised. The electron moves to dot 4. The second and the third rows compare the ladder diagrams of the drag channel with and without Coulomb drag effect, respectively. The second row is the exciton transport regime ($E < V_{ij}$), in which the presence of a drive-channel electron lowers the dot potentials in the drag channel sufficiently for a hole to be loaded in the bottom channel. The hole will then be bound to the electron and travel along with the electron, i.e., an exciton is formed. The third row is the single-electron transport regime ($E > V_{ij}$), in which the charge state in the drag channel is not affected by the drive-channel electron. Note that for simplicity we assume homogeneous $V_{ij} = V$, and the intrachannel and diagonal Coulomb interactions are ignored in the schematics. Also note that while electrons have been added to the first row to make the underlying particle-hole transformation clear, our device can host only holes.

configuration (see the Appendix for the other interchannel pairs). The virtualized sensors result in a gradient-free signal within each charge state region. The interchannel Coulomb interactions $V_{ij}$ between dot $i$ and $j$ are extracted from the size of the anticrossing for an interdot transition. The obtained interchannel Coulomb interaction strengths are $V_{15} = 220$ μeV, $V_{26} = 260$ μeV, $V_{37} = 315$ μeV, and $V_{48} = 213$ μeV. The diagonal Coulomb interactions $V'$ are smaller than 100 μeV.

Figure 3(b) shows the sensor signal as a function of the detuning of dots 1 and 2, $\delta(P'_1 - P'_2)$, and the detuning of dots 5 and 6, $\delta(P'_5 - P'_6)$, near their respective interdot transitions. If we sweep $\delta(P'_1 - P'_2)$ and keep $\delta(P'_5 - P'_6)$ fixed near the 5-6 transition, as indicated by the black arrow in Fig. 3(b), a transition is made from $\binom{0111}{1000}$ to $\binom{1011}{0100}$ whereby a charge tunnels from dot 2 to dot 1 and simultaneously a charge moves from dot 5 to dot 6, thanks to the interchannel Coulomb interactions $V_{15}$ and $V_{26}$. This cotunneling process [49] results in an exciton moving in the ladder array, and is the dominant exciton transport process since it happens before sequential tunneling is energetically allowed (see the path along the black line in Fig. 3).

Efficient exciton transport requires strong intrachannel tunnel couplings in order to obtain large intrachannel cotunneling couplings, and weak interchannel tunnel couplings. Strong interchannel tunneling exceeding the channel detuning would allow the charge carriers to hybridize between the two channels, in which case we can no longer speak of a distinct electron and hole which are bound by long-range Coulomb interaction.

Using the gate voltages, we can control both the interchannel and intrachannel tunnel couplings. The tunnel couplings are characterized by fitting interdot transition sensor signals to a model described in Ref. [61]. Figures 4(a) and 4(b) show the control of $t_{12}$ and $t_{15}$. Because of fabrication procedure, some barrier gates exhibit a weaker response than others, meaning that larger voltage swings are required for modulating the corresponding tunnel couplings (see the Appendix for details). Note that in the virtualized $B'$ we do not compensate for tunnel coupling crosstalk [62,63] since the present experiment requires

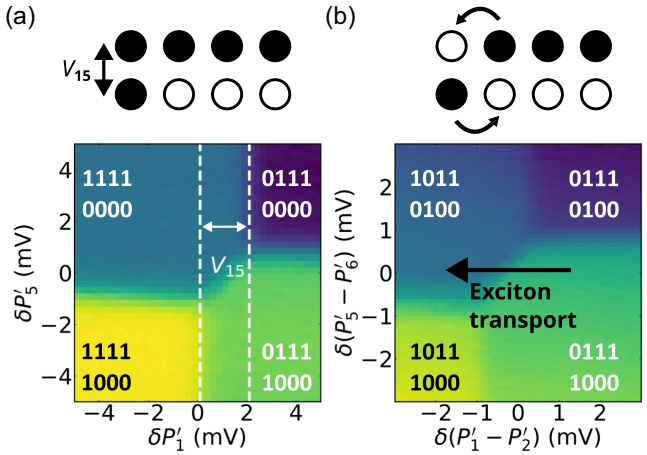


FIG. 3. Charge occupation control of the $4 \times 2$ dot array in the single-hole regime. (a) Charge stability diagram of an interchannel dot pair 1-5. $\delta P_i'$ refers to the change in $P_i'$ relative to a baseline dc voltage. The interchannel Coulomb interaction $V_{15}$, as illustrated in the schematic above, can be determined by measuring the size of the anticrossing (the distance between the white dashed lines) in the charge stability diagrams. The Coulomb interaction strengths are converted from voltage to energy using lever arms. See the Appendix for the charge stability diagrams of all nearest-neighbor dot pairs, for all interchannel Coulomb interaction measurements, and for the extraction of lever arms. (b) Charge stability diagram as a function of 1-2 detuning $\delta(P_1' - P_2')$ and 5-6 detuning $\delta(P_5' - P_6')$. Along the black arrow an exciton moves in the dot array due a cotunneling process depicted in the schematic.

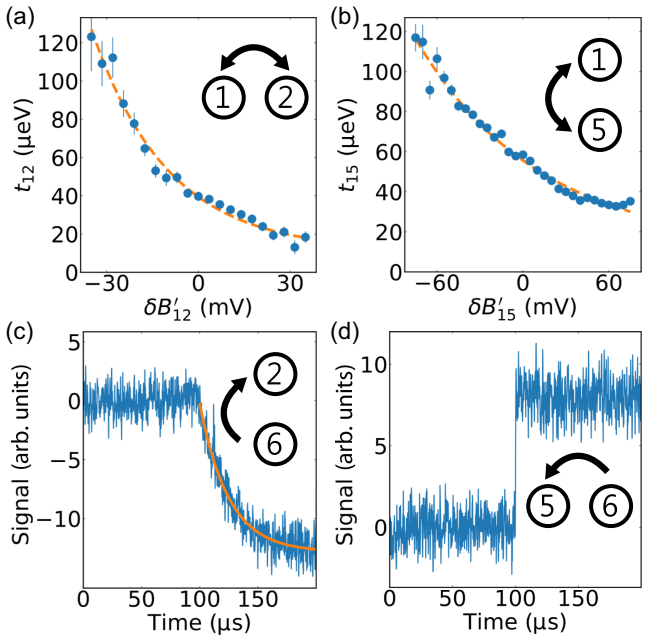


FIG. 4. Tunnel coupling control of the $4 \times 2$ dot array in the single-hole regime. (a),(b) Measurements of (a) intrachannel tunnel coupling $t_{12}$ and (b) interchannel tunnel coupling $t_{15}$ as a function of $B_{12}'$ and $B_{15}'$, respectively. The orange dashed lines show exponential fits to the data. (c) Measurement of tunneling rate $\Gamma_{26}$ between dot 2 and dot 6 when $t_{26}$ is suppressed. A hole is initialized in dot 6 ($\epsilon_6 < \epsilon_2$), and at 100 μs we abruptly align the electrochemical potentials ($\epsilon_6 = \epsilon_2$) using a gate voltage pulse. From this moment, the hole can tunnel from dot 6 to dot 2. The plot shows the time averaged charge sensor response. As expected, we see an exponential trend in the sensor response, since the tunnel time should obey Poisson statistics. The exponential fit yields $\Gamma_{26} = 40$ kHz, which gives a rough estimate of $t_{26} = 0.03$ μeV. (d) Same as (c) but for $\Gamma_{56}$ when $t_{56} = 46$ μeV. $\Gamma_{56}$ is higher than the measurement bandwidth of 1 MHz.

setting the tunnel couplings only once, and furthermore is robust to small variations in tunnel couplings.

We here set all intrachannel tunnel couplings to 30–40 μeV. For the interchannel tunnel couplings we target values ideally below 1 μeV. However, it is challenging to quantify such small tunnel couplings by fitting the interdot sensor signal, given that the thermal energy based on the effective electron temperature is about 20 μeV in this experiment. Instead of the tunnel couplings, we measure the interdot tunnel rates by abruptly aligning the dot potentials using a gate voltage pulse. The relation between tunnel coupling and tunnel rate can be expressed as [64]

$$\Gamma_{ij} = 2T_2 t_{ij}^2, \tag{2}$$

where $\Gamma_{ij}$ and $t_{ij}$ are the tunnel rate and tunnel couplings between dot $i$ and $j$, and $T_2$ is the charge dephasing time ($T_2 \geq 0.3$ ns extracted from photon-assisted tunneling measurement [65]; see the Appendix for details). Figure 4(c) shows the tunnel rate measurement between dot 2 and dot 6. The fit yields $\Gamma_{26} = 40$ kHz. Using Eq. (2) we obtain $t_{26} \leq 0.03$ μeV. For comparison, Fig. 4(d) shows the measurement of $\Gamma_{56}$ when $t_{56} = 46$ μeV. In this case the decay appears instantaneous owing to the fast tunneling between the dots. Using the interchannel barrier voltages, all interchannel tunnel couplings can be suppressed below 0.1 μeV (see the Appendix), with all interchannel Coulomb interactions $> 150$ μeV. However, we ideally want homogeneous interchannel Coulomb interactions of about 200–300 μeV, in order to have a large window for Coulomb drag. Since $V_{15}$ is only 166 μeV when $t_{15} = 0.07$ μeV, we bring dot 1 and dot 5 closer together to increase $V_{15}$ to 220 μeV, at the expense of a higher $t_{15} \sim 25$ μeV [66].

## IV. COULOMB DRAG AND EXCITON FORMATION

The experiment scheme for measuring exciton formation and transport is illustrated in Fig. 2. In phase I, the $4 \times 2$ dot array is set to the $\binom{1111}{0000}$ charge occupation in which the dot potentials in the top channel (drive channel) are aligned and are placed ~200 μeV below the Fermi level. The potentials in the bottom channel (drag channel) are aligned as well,

and positioned above the Fermi level by an energy offset $E$. From phase II to V, the respective top-channel dot potentials are consecutively raised and then lowered by 6 mV (∼670 μeV) to load and shuttle an electron from left to right. If $E < V_{ij}$, the top-channel electron capacitively lowers the bottom-channel potential on the opposite site below the Fermi level. As a consequence a hole is loaded in the bottom channel. Because of the interchannel Coulomb interaction, the hole is dragged along with the electron; i.e., the electron and hole move together as an exciton along the channel throughout the pulse sequence. In contrast, if $E > V_{ij}$, the top-channel electron moves alone without dragging along a hole. Therefore, a transition between exciton transport and single-electron transport is expected to occur at $E \sim V_{\mathrm{av}} = \langle V_{ij} \rangle$. In this work, the average interchannel Coulomb interaction $V_{\mathrm{av}}$ is 252 μeV. We note that for a system with inhomogeneous $V_{ij}$, the range of $E$ where Coulomb drag can occur is limited by the smallest $V_{ij}$.

In the measurements shown in Fig. 5, the top-channel dot potentials are pulsed from phase I to V in the time domain while the bottom-channel potentials are fixed at $E$ [67]. Figures 5(a) and 5(b) show the BL and BR sensor signals as a function of time and $E$. The sensor signals corresponding to the $\binom{1\,1\,1\,1}{0\,0\,0\,0}$ charge state (phase I when $E > 0$) are assigned a reference value of 0. An increasing (decreasing) signal indicates a positive (negative) charge moves closer to the corresponding sensor. In the region enclosed by the blue dashed rectangle, from phase II to V, the BL (BR) sensor signal is increasingly (less and less) negative. As $E$ is reduced, the sensor signals first pass through a transition region around $E \sim 200$ μeV and then reach a region enclosed by the orange rectangle, where the BL (BR) sensor signal is less and less (increasingly) positive from phase II to V.

The data in Figs. 5(a) and 5(b) can be understood as follows. In the blue dashed region, the system is in the single-electron regime in which a top-channel electron is moving away from BL and toward BR. Hence, the magnitude of the negative signal decreases (increases) over time for BL (BR). In contrast, in the orange dashed region, the system enters the exciton transport regime in which an interchannel exciton moves to the right. Because the BL and BR sensors are more sensitive to the bottom-channel hole than to the top-channel electron, the net signal induced by the exciton is positive and the magnitude of this positive signal decreases (increases) over time for BL (BR). See Figs. 5(c) and 5(d) for a further comparison between

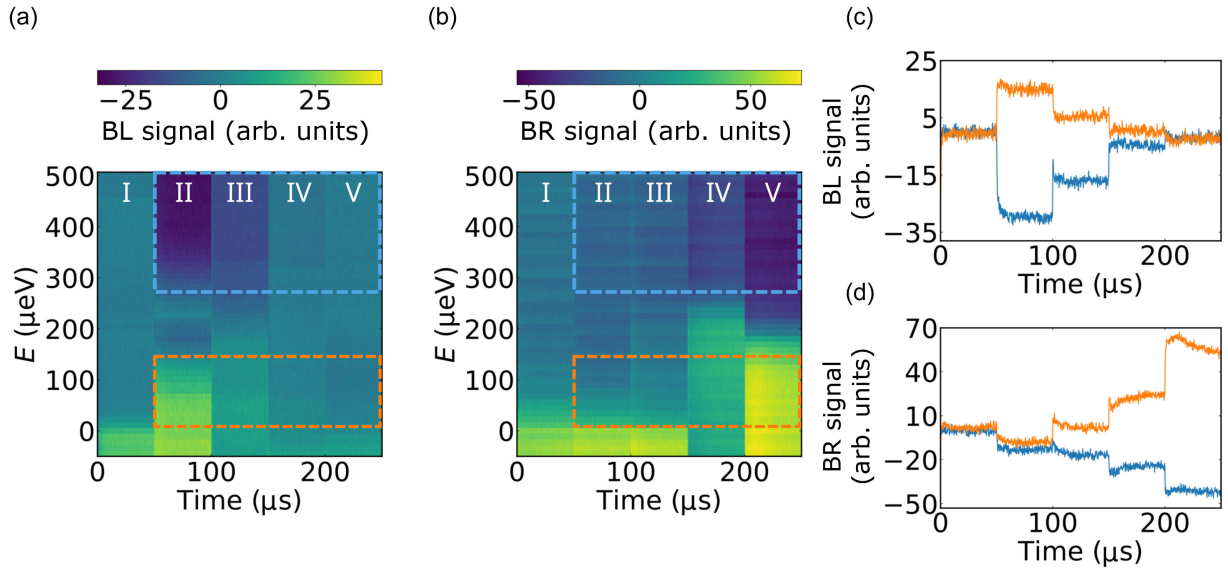


FIG. 5. Coulomb drag and exciton transport measurements. (a) BL and (b) BR processed (see the Appendix) sensor signals as a function of time and $E$. In the time domain the dot potentials in the top channel are pulsed from phase I to V as described in Fig. 2. A positive (negative) charge causes a positive (negative) sensor signal. The regions enclosed by a blue dashed rectangle correspond to the single-electron transport regime, in which only a negative charge moves from the left to the right in the top channel. The regions enclosed by an orange dashed rectangle indicate the exciton transport regime, in which an additional positive charge is loaded and travels with the top-channel electron. Since the BL and BR sensors are more sensitive to charges in the bottom channel than in the top channel, the sensor signals change sign in the exciton transport regime compared to those in the single-electron transport regime. (c) 1D line cuts of the BL sensor signal in the single-electron transport regime ($E \simeq 500$ μeV, blue trace) and in the exciton transport regime ($E \simeq 100$ μeV, orange trace). (d) Same as (c) but for the BR sensor signal. The small drop in the BR signal between 50 and 100 μs is caused by imperfect virtualization of the BR sensor with respect to $P_1'$. The slight bending of the BR signal is possibly caused by charging or discharging of the two-dimensional hole gas (2DHG) near the BR sensor. Additionally, we understand the broadening of the transition line in phase II as a result of strong dot-reservoir coupling.

the signals in the single-electron transport regime and the exciton transport regime. In Figs. 5(a) and 5(b) the transition between the single-electron regime and the exciton transport regime occurs around $E \sim 200$ μeV, which is consistent with the predicted transition point $E \sim V_{\mathrm{av}} = 252$ μeV. The width of the transition regime depends on the level of disorder in the dot potentials ($\delta\epsilon \leq 50$ μeV, which is the accuracy of the automated calibration) and variations in interchannel $V_{ij}$ (standard deviation in $V_{ij}$ of ∼40 μeV). Note that when $E < 0$ μeV, the signals in phase I increase because the bottom channel starts loading holes from the reservoirs, even if no electron is loaded in the top channel.

Finally, since the transport of an interchannel exciton involves a cotunneling process, it is possible in principle that either the electron or the hole or the entire exciton is not successfully transferred from one site to another. In the data of Fig. 5, no such failed charge transfers are observed. This is expected since the 50 μs duration of the pulse segments by far exceeds both the single-particle tunneling rates and the cotunneling rates (in the Appendix, we estimate the probability of successful adiabatic charge transfer to be about 99.2%).

## V. CONCLUSION AND OUTLOOK

In summary, we have fabricated a germanium $4 \times 2$ quantum dot ladder and used it to study exciton formation and transport. To engineer the system Hamiltonian, we tune the full array into the single-hole regime and independently control all the on-site potentials and interdot tunnel couplings. We find strong interchannel Coulomb interaction while the tunneling between channels is suppressed, which is essential for realizing excitonic physics. To probe exciton formation by means of Coulomb drag, we drive an electron through the top channel and measure the charge sensor signals as a function of the bottom-channel potential. The measured signals are in good agreement with the picture of a transition from single-electron transport to exciton transport resulting from the interchannel Coulomb interaction. An interesting next step possible with the present sample is to create and study an engineered excitonic insulator [20].

Whereas tunneling and Coulomb-mediated cotunneling of charges between the dots along each leg of the ladder are quantum mechanical effects, the present experiments on exciton formation and transport can be understood in terms of classical long-range Coulomb interactions without invoking quantum effects (see Appendix A 11). In the future, we envision that with sufficiently homogeneous interaction energies and cotunnel couplings in longer ladders, excitons can delocalize over the array and show both coherent dynamics in the time domain as well as exciton quasicondensation [68]. Already, coherent delocalization of individual charges as well as coherent oscillations of charges in the time domain have been observed previously in quantum dot arrays [10,64,69–73]. Also spin coherence was shown to extend over quantum dot arrays [11,12,63], including across a $4 \times 2$ quantum ladder using a nominally identical device to the one used here [74].

It is useful to point out an enhanced symmetry in bilinear quantum dot arrays as described by Eq. (1), which should play an important role in the nature of the ground state in the thermodynamic limit. As there is no tunneling between the channels, one can define separate SU(2) symmetries for each channel [75]. The full Hamiltonian is symmetric with respect to both of them, and the full symmetry of the system is $\mathrm{SO}(4) \simeq \mathrm{SU}(2) \otimes \mathrm{SU}(2)$ [76]. Excitonic condensation in this system would require spontaneous symmetry breaking of the SO(4) symmetry. For non-Abelian symmetries such as SO(4), the Hohenberg-Mermin-Wagner theorem shows that only exponentially decaying correlations are allowed even at zero temperature, due to the abundance of possible fluctuations of the order parameter. This should be contrasted to the excitonic states of spinless fermions, for which condensation corresponds to the Abelian U(1) symmetry and thus the system can exhibit quasi-long-range at zero temperature in one-dimensional systems.

Interestingly, two excitons can together form a SO(4) singlet. Such singlets can exhibit quasi-long-range order at zero temperature in one-dimensional systems, analogously to spinless bosons. This suggests our system can exhibit unusual types of ground states in the thermodynamic limit, such as quasicondensates of composite particles or states with broken translational symmetry. Analogous phenomena have been discussed in the context of spinor condensates of cold atoms in one-dimensional systems [77,78].

One can also break the SO(4) symmetry by introducing extra terms to the Hamiltonian. When breaking SO(4) symmetry with a magnetic field, $S_z = 1$ excitons are favored and can form a (quasi)condensate, which is not usually seen in optical spectroscopy since these excitons are dark. In addition, the spin-orbit coupling present in germanium quantum wells, while not breaking time reversal symmetry [79], can also hybridize singlet and triplet states, lifting their degeneracy [80,81], which may lead to condensation at zero magnetic field.

Owing to the *in situ* tunability of device parameters, the quantum dot platform offers access to a wide variety of regimes. For instance, a transition from semiconductor to excitonic insulator can be observed by changing the detuning between two channels. The BCS-BEC crossover might be realized by increasing the exciton density while fixing the Coulomb interaction strength [82]. Moreover, one may create and manipulate charged excitons (trions) by introducing imbalanced electron and hole numbers in the channels. Another important regime for the SO(4) physics in 1D systems is the so-called "incoherent Luttinger liquid" regime [83], where the temperature is below the charge (exciton in our case) binding energy but above the spin interaction energy. In this case, we expect Luttinger liquid

power-law correlations in the "exciton number" but short-range correlations in the spin sector.

The data reported in this paper are archived on a Zenodo data repository [84].

## ACKNOWLEDGMENTS

We acknowledge useful discussions with members of the Vandersypen group, and with D. Sels, S. Gopalakrishnan, A. Bohrdt, F. Grusdt, I. Morera, and H. Lange. We thank software development by S. L. de Snoo. We also acknowledge technical support by O. Benningshof, J. D. Mensingh, R. Schouten, E. Van der Wiel, and N. P. Alberts. L. M. K. V. acknowledges support from an Advanced Grant of the European Research Council (ERC) under the European Union's Horizon 2020 research and innovation programme (Grant Agreement No. 882848) and by a Vici grant of the Dutch Research Council (NWO). E. D. acknowledges support from the Army Research Office (ARO) Grant No. W911NF-20-1-0163, the SNSF Project No. 200021-212899, and the Swiss State Secretariat for Education, Research and Innovation (SERI) under Contract No. UeM019-1.

## APPENDIX

### 1. Device fabrication and experiment setup

The device was fabricated on a Ge/SiGe heterostructure featuring a strained Ge quantum well positioned 55 nm below the semiconductor-dielectric interface, as described in Ref. [60]. The fabrication started by defining Ohmic contacts, which were made by electron beam lithography, etching of the native oxide with buffered hydrofluoric acid (HF), and electron beam deposition of 30 nm of Al. An insulating layer of 7 nm $Al_2O_3$ was grown with atomic layer deposition (ALD), also annealing the device and diffusing the aluminum into the heterostructure during the process. Subsequently, the screening gates (3/17 nm Ti/Pd), plunger gates (3/27 nm Ti/Pd), and barrier gates (3/37 nm Ti/Pd) were made in three metalization layers, which are all separated by 5-nm-thick layers of $Al_2O_3$. Note that for easing the lift-off of the compact barrier gates, we made the barrier gates in two steps, in which the barrier gates were distributed in two lithography-evaporation-lift-off processes without a $Al_2O_3$ layer in between. The fabrication procedure is summarized in Fig. 6. The chosen device design provides a scalable path to longer bilinear quantum dot arrays with full control over all dot potentials and interdot tunnel couplings. Charge sensing can be accomplished dispersively or with sensors integrated alongside the ladder instead of at the extremities only.

The measurement was performed in an Oxford Instruments Triton dilution refrigerator with a nominal base temperature of 6 mK. The device was mounted on a custom-made sample printed circuit board (PCB). dc voltages from homebuilt serial peripheral interface (SPI) DAC modules and pulses from a Keysight M3202A arbitrary waveform generator are combined using

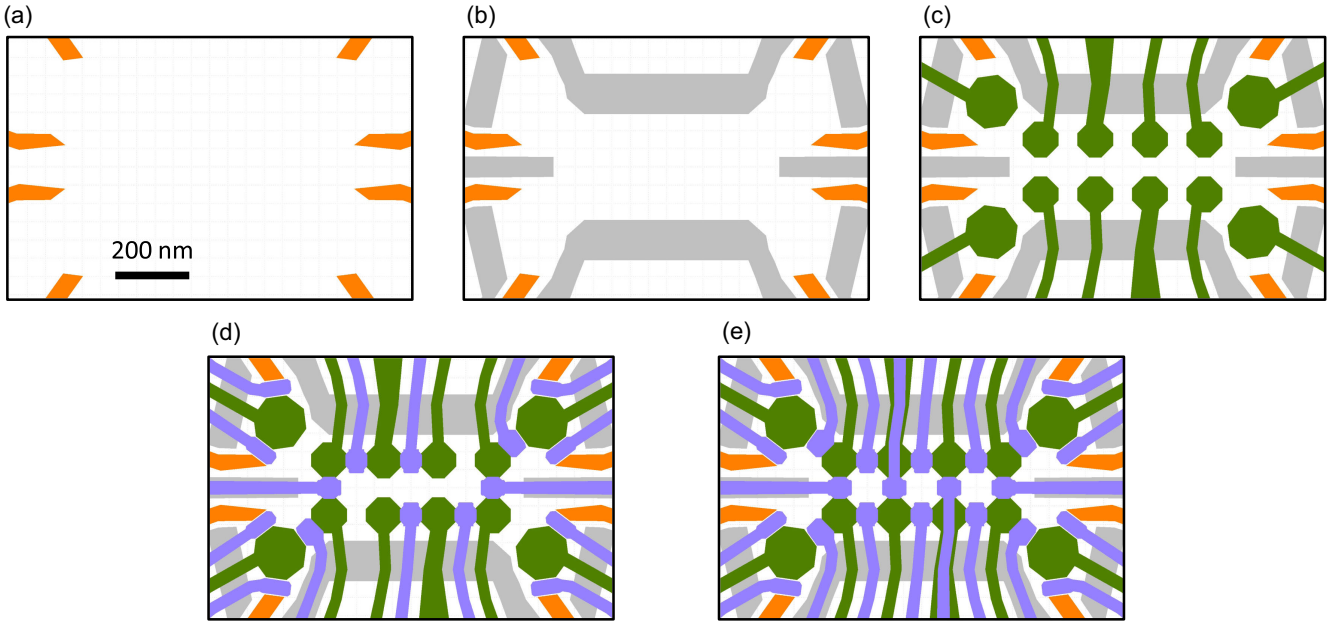


FIG. 6. Fabrication steps for the 4 × 2 Ge quantum dot ladder, showing the design of each patterned layer. (a) Ohmic contact layer for contacting the Ge quantum well. (b) Screening gate layer for defining the active region in which holes are confined. (c) Plunger gate layer for charge accumulation and electrochemical potential control. (d),(e) First and second barrier layer used for shaping the quantum dot potentials and for tunnel coupling control. The layers in (a)–(d) are separated by $Al_2O_3$ insulating layers. The barrier gates in (d) and (e) are realized in two separate metalization steps (with no insulating layer in between) to ease the lift-off process.

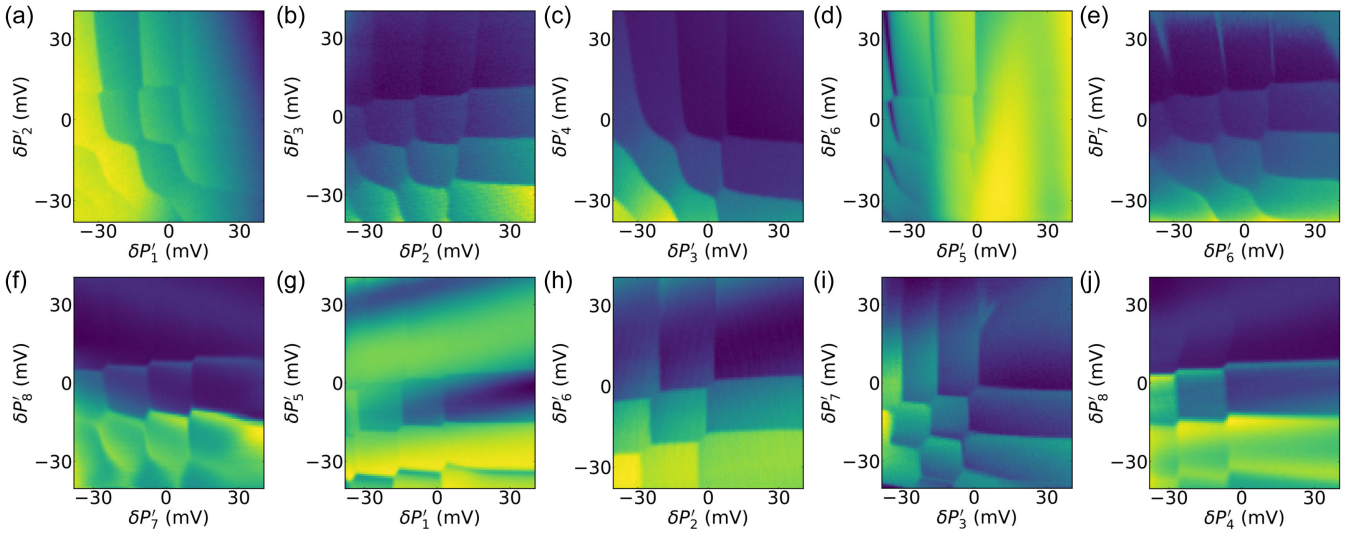


FIG. 7. Charge stability diagrams of all neighboring dot pairs, showing the left or right bottom sensor signal as a function of two virtual plunger gate voltages. (a)–(f) Dot pairs along the top or bottom channel. (g)–(j) Dot pairs across the channel. The top right corner of each figure corresponds to the zero-charge state. Note that at this tuning stage, there existed a strong coupling between dot 5 and BL sensor, which resulted in an improper virtualization and reduced sensitivity when dot 5 was empty. However, this problem was solved with further tuning. See Fig. 3, where all relevant addition and interdot lines as well as the proper sensor virtualization are clearly visible for dots 1 and 5.

on-PCB bias tees. rf reflectometry for charge sensing was done using SPI in-phase and quadrature (IQ) demodulation modules and on-PCB *LC* tank circuits. The demodulated signals were recorded by a Keysight M3102A digitizer.

### 2. Single-hole regime of the $4 \times 2$ array

The charge state tunability of the $4 \times 2$ ladder is displayed in Fig. 7, where we show charge stability diagrams for all dot pairs down to the single-hole regime. The area on the top right corner of the plots corresponds to the zero-charge state. The effect of gate voltage crosstalk is compensated using virtual gates $P'$. All ten plots are obtained using charge sensing using the bottom right and bottom left sensors.

Additionally, in Fig. 8, we show global charge state control of full the $4 \times 2$ array by sweeping two virtual gates, corresponding to the top and bottom channel energies ($P_T$ and $P_B$, respectively). Every vertical or horizontal addition line reflects a single charge being added to either the top or the bottom channel. Lines are spaced apart by the long-range Coulomb interaction. The starting charge occupation for the Coulomb drag experiment corresponds to the top left of this plot, with four charges in the top channel and none in the bottom.

### 3. Lever arm measurement

The conversion between a virtual gate voltage $P_i'$ and electrochemical potential $\epsilon_i$ is described by $\delta\epsilon_i = L_i \delta P_i'$, where $L_i$ is the lever arm for dot $i$. The lever arms can be characterized using photon-assisted tunneling (PAT) [65]. In Fig. 9(a), the signal is fitted to $hf = \sqrt{\delta\epsilon_3^2 + 4t_{37}^2}$. From the fit a lever arm $L_3 = 117\ \mu\text{eV/mV}$ is extracted. In addition, the ratio between two lever arms can be determined from the slope $S$ of an interdot charge transition line based on the fact that $V_{ij} = V_{ji}$. For instance, in Fig. 9(b), $V_{34} = L_3 H = V_{43} = L_4 W$. Therefore, $S = H/W = L_4/L_3$. So, $L_4$ can be estimated from $L_3$ and $S$. We obtain $L_4 = 117\ \mu\text{eV/mV}$ with $L_3 = 117\ \mu\text{eV/mV}$ and $S = 1.0$. Similarly, based on PAT measurements and interdot slopes, all lever arms are estimated. The results are summarized in Table I. All lever arms have similar value $\sim 110\ \mu\text{eV/mV}$ with a standard deviation of $4\ \mu\text{eV/mV}$.

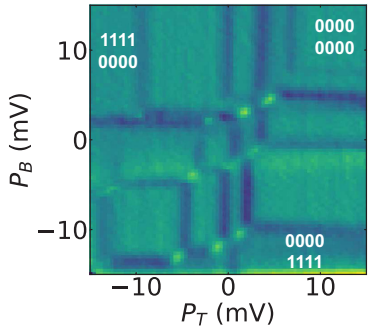


FIG. 8. Charge stability diagram depicting the global charge state tunability of the $4 \times 2$ array. The scanned gates are the top and bottom channel virtual voltage $P_T = P_1' + P_2' + P_3' + P_4'$ and $P_B = P_5' + P_6' + P_7' + P_8'$. Every vertical (horizontal) charge transition corresponds to adding a single charge to the top (bottom) channel. We plot the gradient of the sensor signal for better resolution of the transition lines. The top left region of this plot corresponds to a filled top channel and an empty bottom channel, which is the starting charge configuration for the Coulomb drag experiment.

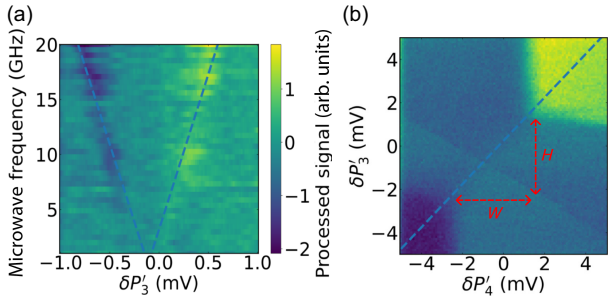


FIG. 9. Example of lever arm measurements. (a) PAT measurement showing the processed sensor signal as a function of frequency and detuning at the interdot transition between dot 3 and dot 7. The blue dashed line is a fit of the form $hf = \sqrt{\delta\epsilon_3^2 + 4t_{37}^2}$, where $\delta\epsilon_3 = L_3\delta P_3'$. The linewidth is about 0.1 mV (11.7 μeV), from which we estimate a charge coherence time $T_2 \geq 0.3$ ns. (b) The charge stability diagram at the interdot transition between dot 3 and dot 4. The blue dashed line shows the interdot transition line with a slope $S = H/W = L_4/L_3$, where $H$ is the height and $W$ is the width of the transition line.

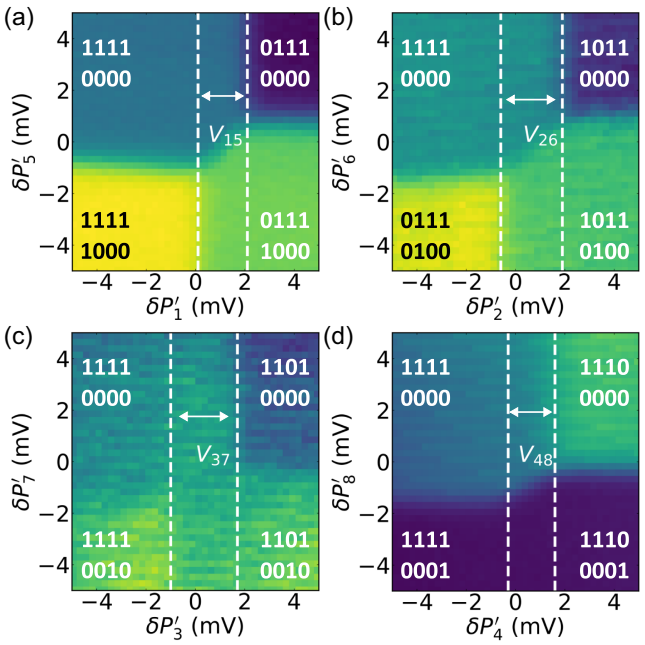


FIG. 10. Measurements of interchannel Coulomb interactions (a) $V_{15}$ [replotted from Fig. 3(a)], (b) $V_{26}$, (c) $V_{37}$, and (d) $V_{48}$.

### 4. Interchannel Coulomb interaction measurement

Figures 10(a)–10(d) show the measurements of interchannel Coulomb interactions, which are responsible for the excitonic Coulomb drag effect. As in Fig. 3(a), the Coulomb interactions are characterized by finding the sizes of the anticrossings and converting them into energies through lever arms. From Figs. 10(a)–10(d) we obtain $V_{15} = 220$ μeV, $V_{26} = 260$ μeV, $V_{37} = 315$ μeV, and $V_{48} = 213$ μeV.

### 5. Tunnel coupling control

Figure 11 shows control of all nearest-neighbor tunnel couplings $t_{ij}$ using the corresponding virtual barrier gates $B_{ij}'$. The tunnel coupling dependency is fitted by an exponential function $A\exp(-\gamma_{ij}B_{ij}') + C$, from which the barrier lever arm $\gamma_{ij}$ is extracted. The $\gamma_{ij}$ are summarized in Table II. Roughly, the barrier lever arms can be separated into two groups, corresponding to the two steps in which the barriers were fabricated. Notably, the barrier gates patterned in the first fabrication step display a stronger lever arm than those patterned in the second step, despite the absence of an ALD layer between the two barrier metalization layers. The reasons for this discrepancy require further investigation, but might be caused by the device design or residual resist under the second barrier gate layer. Nonetheless, all barriers display a reasonable level of tunnel coupling control, which allows us to tune the tunnel couplings to the values required to perform the excitonic Coulomb drag experiment.

TABLE I. The values and measurement methods for each lever arm $L_i$.

| $L_i$ | Value (μeV/mV) | Method |
|---|---|---|
| $L_1$ | 111 | Interdot slope |
| $L_2$ | 104 | PAT |
| $L_3$ | 117 | PAT |
| $L_4$ | 117 | Interdot slope |
| $L_5$ | 115 | Interdot slope |
| $L_6$ | 113 | PAT |
| $L_7$ | 112 | PAT |
| $L_8$ | 111 | Interdot slope |

### 6. Tunnel rate measurement

Tunnel coupling extraction via fitting of the interdot transition signals allows us to reliably obtain tunnel coupling values of the order of tens of μeV, larger than or comparable to the electron temperature. As $t_{ij}$ becomes much smaller than the electron temperature, this fit becomes unreliable. When the hopping between channels is suppressed, we estimate the interchannel $t_{ij}$ from the interchannel tunnel rates $\Gamma_{ij}$ as described in the main text. Figures 12(a)–12(d) show the tunnel rate measurements, from which we obtain $\Gamma_{15} = 208$ kHz, $\Gamma_{26} = 40$ kHz, $\Gamma_{37} = 118$ kHz, and $\Gamma_{48} = 81$ kHz. Since we estimate $T_2 \geq 0.3$ ns (lower limit) from the linewidth of the PAT in Fig. 9(a), by using Eq. (2) we can then estimate $t_{15} \leq 0.07$ μeV, $t_{26} \leq 0.03$ μeV, $t_{37} \leq 0.06$ μeV, and $t_{48} \leq 0.05$ μeV in the target regime where the interchannel hopping is suppressed.

### 7. Automated calibration routine

Slow changes in the electrostatic environment of the device lead to inevitable drift of dot electrochemical

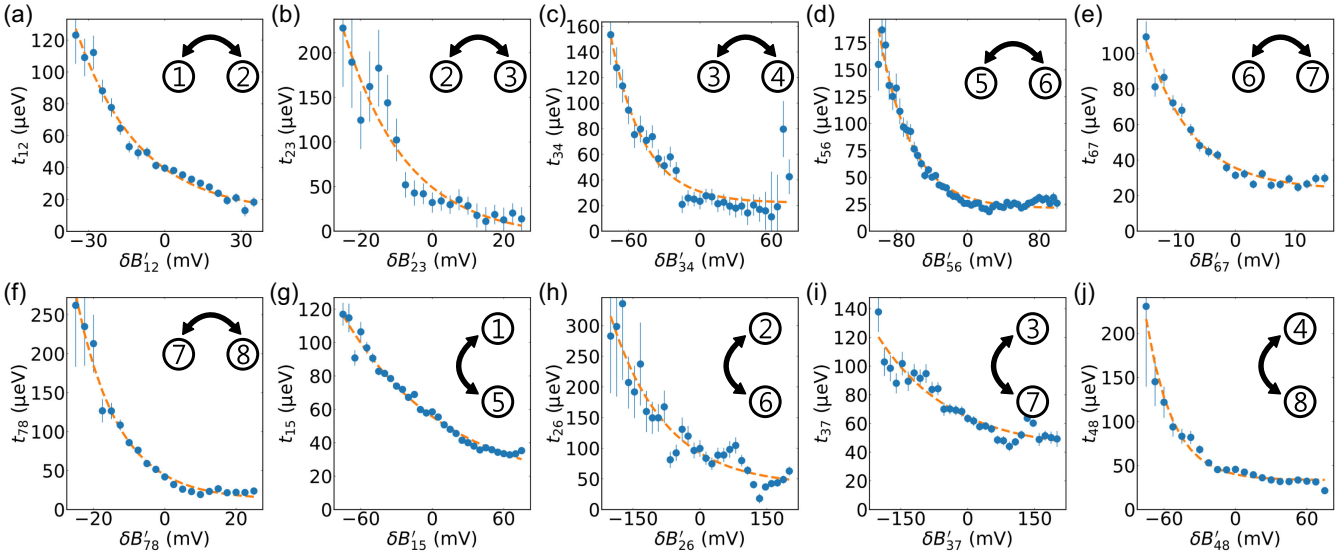


FIG. 11. Control of all nearest-neighbor tunnel couplings. (a)–(f) Measured intrachannel tunnel coupling $t_{ij}$ as a function of virtual barrier gates $B'_{ij}$. (g)–(j) Measured interchannel tunnel coupling $t_{ij}$ as a function of virtual barrier gates $B'_{ij}$. The orange dashed lines are exponential fits to the data.

potentials. To compensate for this low frequency drift, we implement a fast automated calibration routine to keep the electrochemical potentials fixed relative to the Fermi level. Our target is to set the level of dot $i$ with an offset $P'_{i,\mathrm{target}}$ from the Fermi level. In this experiment $P'_{1,\mathrm{target}}$ to $P'_{8,\mathrm{target}}$ are initially $[2, 2, 2, 2, -4, -4, -4, -4]$ mV, which places the device in the $\binom{1111}{0000}$ charge state. For the first instance of the calibration, we manually tune the device to a baseline dc voltage $V_{\mathrm{base}}$ close to the target condition (within a tolerance of a few mV). The calibration routine starts with optimizing the sensor signals, which is done by scanning sensor plunger gates and locating the optimal sensing positions, as shown in Figs. 13(a) and 13(f). The voltage drift of dot $i$ is measured by scanning $P'_i$ centered at $V_{\mathrm{base}} + P'_{i,\mathrm{target}}$ and fitting the signal to a charge addition line to locate the Fermi level, as shown in Figs. 13(b)–13(e) and 13(g)–13(j). $V_{\mathrm{base}}$ is subsequently shifted by the deviation of the addition lines from the centers of the scans to compensate for the voltage drift. The entire automated calibration routine takes about 10 s and offers a valuable tool for the efficient adjustment of dot potentials in multidot devices.

TABLE II. The values and corresponding barrier fabrication steps for each tunnel barrier lever arm $\gamma_{ij}$.

| $\gamma_{ij}$ | Value (1/mV) | Barrier fabrication step |
|---|---|---|
| $\gamma_{12}$ | 0.040 | First |
| $\gamma_{23}$ | 0.057 | First |
| $\gamma_{34}$ | 0.036 | Second |
| $\gamma_{56}$ | 0.028 | Second |
| $\gamma_{67}$ | 0.128 | First |
| $\gamma_{78}$ | 0.085 | First |
| $\gamma_{15}$ | 0.012 | First |
| $\gamma_{26}$ | 0.008 | Second |
| $\gamma_{37}$ | 0.006 | Second |
| $\gamma_{48}$ | 0.044 | First |

### 8. Exciton tunnel coupling

The tunneling of excitons entails a cotunneling process of two charges in the ladder array. Here we take the tunneling between $\binom{1011}{0100}$ and $\binom{1101}{0010}$ as an example. The relevant charge states are $|0\rangle = \binom{1011}{0100}$, $|1\rangle = \binom{1101}{0010}$, $|2\rangle = \binom{1101}{0100}$, $|3\rangle = \binom{1011}{0010}$, $|4\rangle = \binom{1111}{0000}$, and $|5\rangle = \binom{1001}{0110}$. The Hamiltonian in this basis is

$$H = \begin{pmatrix} E_0 & 0 & -t_{23} & -t_{67} & -t_{26} & -t_{37} \\ 0 & E_1 & -t_{67} & -t_{23} & t_{37} & t_{26} \\ -t_{23} & -t_{67} & E_2 & 0 & 0 & 0 \\ -t_{67} & -t_{23} & 0 & E_3 & 0 & 0 \\ -t_{26} & t_{37} & 0 & 0 & E_4 & 0 \\ -t_{37} & t_{26} & 0 & 0 & 0 & E_5 \end{pmatrix}, \quad \text{(A1)}$$

where

$$\begin{aligned} E_0 &= -\epsilon_3 - \epsilon_6 + V + 2V' - \epsilon_1 - \epsilon_4, \\ E_1 &= -\epsilon_2 - \epsilon_7 + V + 2V' - \epsilon_1 - \epsilon_4, \\ E_2 &= -\epsilon_2 - \epsilon_6 + 2V + V' - \epsilon_1 - \epsilon_4, \\ E_3 &= -\epsilon_3 - \epsilon_7 + 2V + V' - \epsilon_1 - \epsilon_4, \\ E_4 &= -\epsilon_2 - \epsilon_3 + 3V - \epsilon_1 - \epsilon_4, \\ E_5 &= -\epsilon_6 - \epsilon_7 + V + 2V' - \epsilon_1 - \epsilon_4. \end{aligned} \quad \text{(A2)}$$

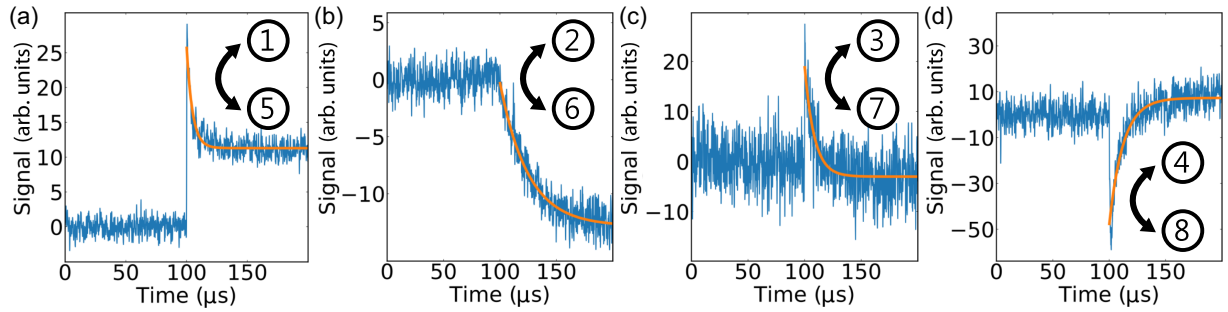


FIG. 12. Tunnel rate measurements for (a) $\Gamma_{15}$, (b) $\Gamma_{26}$, (c) $\Gamma_{37}$, and (d) $\Gamma_{48}$. The orange curves are exponential fits to the data.

$V$ the nearest-neighbor Coulomb interaction and $V'$ the diagonal Coulomb interaction (for simplicity we assume homogeneous $V$ and $V'$ in the ladder array). Near a symmetric exciton tunneling condition in which $\epsilon_2 \approx \epsilon_3 = \epsilon + \Delta$, $\epsilon_6 \approx \epsilon_7 = \epsilon$, and $(V - V'), \Delta \gg t_{23}, t_{67}, t_{26}, t_{37}$, Eq. (A2) becomes

$$\begin{aligned}
E_0 &= -2\epsilon - \Delta + V + 2V' + \delta E_0,\\
E_1 &= -2\epsilon - \Delta + V + 2V' + \delta E_1,\\
E_2 &= -2\epsilon - \Delta + 2V + V' + \delta E_2,\\
E_3 &= -2\epsilon - \Delta + 2V + V' + \delta E_3,\\
E_4 &= -2\epsilon - 2\Delta + 3V + \delta E_4,\\
E_5 &= -2\epsilon + V + 2V' + \delta E_5,
\end{aligned} \tag{A3}$$

where $\delta E_i$ is a small perturbation of $E_i$ near the symmetric exciton tunneling condition. We then express Eq. (A1) in the eigenbasis of the first-order perturbation $H' \simeq U^\dagger H U$, in which

$$U = \begin{pmatrix}
1 & 0 & -\frac{t_{23}}{V-V'} & -\frac{t_{67}}{V-V'} & -\frac{t_{26}}{2V-2V'-\Delta} & -\frac{t_{37}}{\Delta}\\
0 & 1 & -\frac{t_{67}}{V-V'} & -\frac{t_{23}}{V-V'} & \frac{t_{37}}{2V-2V'-\Delta} & \frac{t_{26}}{\Delta}\\
\frac{t_{23}}{V-V'} & \frac{t_{67}}{V-V'} & 1 & 0 & 0 & 0\\
\frac{t_{67}}{V-V'} & \frac{t_{23}}{V-V'} & 0 & 1 & 0 & 0\\
\frac{t_{26}}{2V-2V'-\Delta} & -\frac{t_{37}}{2V-2V'-\Delta} & 0 & 0 & 1 & 0\\
\frac{t_{37}}{\Delta} & -\frac{t_{26}}{\Delta} & 0 & 0 & 0 & 1
\end{pmatrix}. \tag{A4}$$

Neglecting terms of more than second order in $t_{ij}/V - V'$, $t_{ij}/2V - 2V' - \Delta$, or $t_{ij}/\Delta$, the effective Hamiltonian $H'$ for the perturbed states $|0'\rangle$ and $|1'\rangle$ becomes

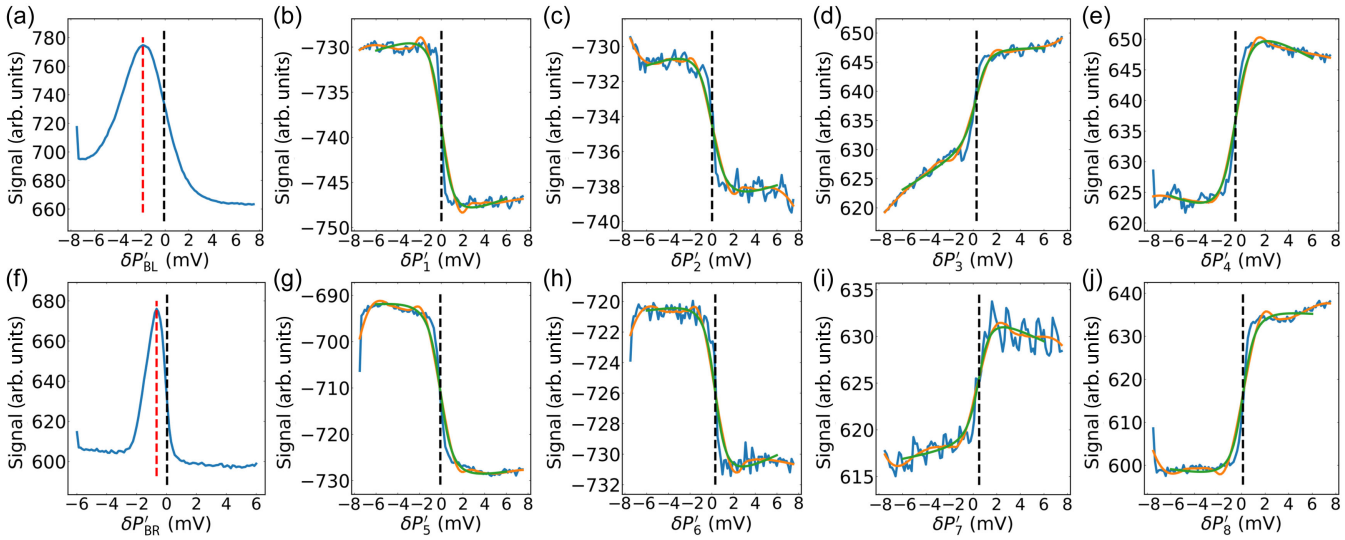


FIG. 13. Fast automated calibration routine. Panels (a) and (f) show the sensor signals as a function of sensor plunger gates $P'_{BL}$ (BL sensor) and $P'_{BR}$ (BR sensor). The red dashed lines indicate the sensor peak positions and the black dashed lines indicate the optimal sensing positions (where the slope is steepest). $P'_{BL}$ and $P'_{BR}$ are subsequently moved to the optimal sensing positions. Panels (b)–(e) and (g)–(j) are the sensor signals for dot 1 to 8, near the addition lines for the first hole of each dot. The black dashed lines show the voltages at which $\epsilon_i$ aligns with the Fermi level. Note that (b)–(e) and (g)–(j) are not centered at the same dc voltages. Instead, each addition line is taken with an added offset $\Delta P'_{i,\text{target}}$ from the original dc voltage $V_{\text{base}}$. $V_{\text{base}}$ is then adjusted according to the deviation of the black dashed lines from the centers of the scans. Each scan takes approximately 1 s and the whole calibration routine takes about 10 s.

$$H' = \begin{pmatrix} E_{0'} & -t_{\mathrm{co}} \\ -t_{\mathrm{co}} & E_{1'} \end{pmatrix}, \tag{A5}$$

where $E_{0'} = E_0 - (t_{23}^2/V - V') - (t_{67}^2/V - V') - (t_{26}^2/2V - 2V' - \Delta) - (t_{37}^2/\Delta)$, $E_{1'} = E_1 - (t_{23}^2/V - V') - (t_{67}^2/V - V') - (t_{37}^2/2V - 2V' - \Delta) - (t_{26}^2/\Delta)$, and $t_{\mathrm{co}} = 2(t_{23}t_{67}/V - V') - (t_{26}t_{37}/2V - 2V' - \Delta) - (t_{26}t_{37}/\Delta)$ [64]. From Eq. (A5) we see that the tunneling of exciton states is determined by $t_{\mathrm{co}}$, which has a term proportional to the product of intrachannel tunnel couplings and a term proportional to the product of interchannel tunnel couplings. In the present experiment, the former is much larger than the latter by at least 3 orders of magnitude. Therefore, $t_{\mathrm{co}}$ is predominantly caused by the cotunneling of charges in the intrachannel direction.

### 9. Adiabatic exciton transfer probability

We estimate the probability that an exciton adiabatically transitions between neighboring sites in the quantum dot ladder. When this transition does not occur adiabatically, the exciton initially stays where it was. Afterward, either the electron or the hole may tunnel, leaving the other particles behind, and eventually the entire exciton may still transition, but at least for a brief moment in time the intended exciton transport does not take place. For instance, the transition from $\left(\begin{smallmatrix}1&0&1&1\\0&1&0&0\end{smallmatrix}\right)$ to $\left(\begin{smallmatrix}1&1&0&1\\0&0&1&0\end{smallmatrix}\right)$ might instead end with $\left(\begin{smallmatrix}1&0&1&1\\0&1&0&0\end{smallmatrix}\right)$ (the pair is not transferred) or $\left(\begin{smallmatrix}1&1&0&1\\0&1&0&0\end{smallmatrix}\right)$ (a hole lags behind). Using the Landau-Zener formula [85,86], we obtain

$$\begin{aligned} P_{\mathrm{dia}} &= \exp\left(-2\pi \frac{t_{\mathrm{co}}^2}{\hbar V_E}\right), \\ t_{\mathrm{co}} &= \frac{2t^2}{V - V'}, \\ V_E &= \frac{\Delta E}{\Delta T_r}, \end{aligned} \tag{A6}$$

where $P_{\mathrm{dia}}$ is the diabatic transition probability for the transition from $\left(\begin{smallmatrix}1&0&1&1\\0&1&0&0\end{smallmatrix}\right)$ to $\left(\begin{smallmatrix}1&1&0&1\\0&0&1&0\end{smallmatrix}\right)$, $t_{\mathrm{co}}$ is the intrachannel cotunneling of the electron-hole pair, $V_E$ is the energy level velocity, $t$ is the intrachannel tunnel coupling, $V$ is the interchannel Coulomb interaction, $V'$ is the diagonal Coulomb interaction, $\Delta E$ is the energy difference between the $\left(\begin{smallmatrix}1&0&1&1\\0&1&0&0\end{smallmatrix}\right)$ and $\left(\begin{smallmatrix}1&1&0&1\\0&0&1&0\end{smallmatrix}\right)$ charge states, and $\Delta T_r$ is the rise time of the pulse. Note that we do not include the interchannel cotunneling processes in the analysis because they are at least 3 orders of magnitude smaller than that of the intrachannel cotunneling process, as discussed before. Entering the experimental parameters, we obtain $P_{\mathrm{dia}} \simeq 0.8\%$. Therefore, during Coulomb drag the interchannel exciton is transported adiabatically with an estimated fidelity of 99.2%.

At this point, it is worth mentioning the effect of electron temperature to the exciton transfer fidelity. While the measured temperature of 20 μeV is much larger than the interchannel tunnel coupling, it is still an order of magnitude smaller than the exciton transport window of about 200 μeV. Operation in the exciton transport regime is possible by choosing a global detuning point which is substantially far away from any transition line [see Figs. 5(c) and 5(d); line cuts taken at a distance of 100 μeV from the Fermi energy]. Additionally, the interchannel tunnel rates extracted from Fig. 12 naturally include the effect of thermal excitations. Therefore, when the two channels are aligned, the thermal hopping strength is at least below the extracted tunnel rates of below 210 kHz. This translates to an interdot tunnel coupling strength of below 0.1 μeV, which is much weaker than all other tunneling and cotunneling coupling strengths.

### 10. Coulomb drag data processing

In Fig. 5 the raw data of the BR sensor signal is inverted such that an increasing (decreasing) signal corresponds to a

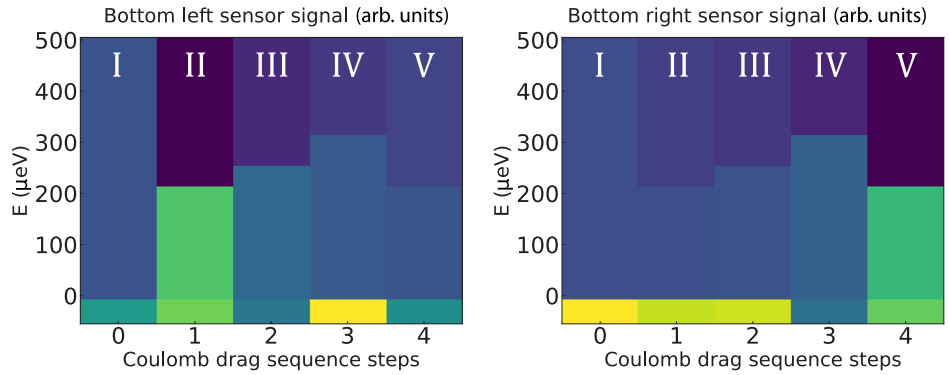


FIG. 14. Numerical simulation of exciton transport measurements. The simulation calculates the ground state charge configuration as a function of electrochemical potentials $\{\epsilon_i\}$. At every Coulomb drag step, the corresponding dot potential is pulsed by 670 μeV as specified in the main text. The simulation uses the measured $V_{ij}$ and assumes slightly larger intrachannel Coulomb interaction terms of 400 μeV. Further, we input $U_i = 2000$ μeV and neglect next-nearest-neighbor interactions. The calculated charge state is transformed to sensor signal assuming a linear sensor response and a $1/r^2$ decay of interactions over distance. The simulation data are in good agreement with the measured data [Fig. 5(a)].

positive (negative) charge. In addition, residual crosstalk from the bottom virtual gates to the sensor signals leads to a small gradient along $E$ ($y$ axis) in phase I of Figs. 5(a) and 5(b). We remove this residual crosstalk by fitting the signals in phase I to a linear background signal and subtracting this background from the data of the entire panel. The scripts for data processing can be found in the data repository [84].

### 11. Numerical simulation of exciton transport

We perform numerical simulations to compare with the measured exciton transport data in Figs. 5(a) and 5(b). To this end, we compute the ground state charge configuration of a classical Fermi-Hubbard Hamiltonian:

$$H = \sum_i \epsilon_i n_i + U \sum_i \frac{n_i(n_i-1)}{2} + U' \sum_{\langle i,j \rangle} n_i n_j + \sum_{i\in\alpha, j\in\beta} V_{ij} n_i n_j + V' \sum_{i\in\alpha, j\in\beta} n_i n_j. \tag{A7}$$

Compared to Eq. (1), we have set $t = 0$ to facilitate the computation. We further include the electrochemical potentials $\{\epsilon_i\}$ and account for the experimentally observed differences in interchannel Coulomb repulsion $V_{ij}$.

Because of the absence of tunnel coupling terms, this simple Hamiltonian is already diagonal. Finding its ground state charge configuration becomes therefore a straightforward energy minimization problem. Since $U \gg V_{ij}, U'$, double occupations are always high in energy and it suffices to input homogeneous charging energies $U \sim 2$ meV as extracted from charge stability diagrams in Fig. 7. To capture the observed variations of the exciton transport windows, it is necessary to input the measured interchannel Coulomb interaction parameters $V_{ij}$ as specified in the main text (see Sec. IV, neglecting diagonal interactions). Furthermore, for the intrachannel Coulomb interaction, we assume homogeneous interaction terms $U' \sim 400$ μeV.

Figure 14 shows the simulated charge ground state variation as a function of the electrochemical potentials $\{\epsilon_i\}$. These are varied in the same way as in the experiment: The bottom (drag) channel detuning $E$ is swept from 500 μeV to past the Fermi energy, while the individual top-channel potentials are raised and lowered by 670 μeV, corresponding to the charge shuttling sequence specified in Sec. IV. The charge states are converted to charge sensor signal by inputting the sensor-to-dot distances $\{r_i\}$ and assuming $1/r^2$ decay of Coulomb interactions and a linear response of the sensors. The numerical simulations show good agreement with the measured data. We point out that for each dot pair, the exciton transport window is equal to the interchannel Coulomb interaction $V_{ij}$, as highlighted in the main text. The faster vanishing response of the measured data as opposed to the numerical simulations can be explained by a decay of Coulomb interactions faster than $1/r^2$, as previously observed in other work [87].


[1] J. I. Cirac and P. Zoller, *Goals and opportunities in quantum simulation*, Nat. Phys. **8**, 264 (2012).

[2] I. M. Georgescu, S. Ashhab, and F. Nori, *Quantum simulation*, Rev. Mod. Phys. **86**, 153 (2014).

[3] P. Barthelemy and L. M. K. Vandersypen, *Quantum dot systems: A versatile platform for quantum simulations*, Ann. Phys. (Berlin) **525**, 808 (2013).

[4] E. Manousakis, *A quantum-dot array as model for copper-oxide superconductors: A dedicated quantum simulator for the many-fermion problem*, J. Low Temp. Phys. **126**, 1501 (2002).

[5] T. Byrnes, N. Y. Kim, K. Kusudo, and Y. Yamamoto, *Quantum simulation of Fermi-Hubbard models in semiconductor quantum-dot arrays*, Phys. Rev. B **78**, 075320 (2008).

[6] S. Yang, X. Wang, and S. Das Sarma, *Generic Hubbard model description of semiconductor quantum-dot spin qubits*, Phys. Rev. B **83**, 161301(R) (2011).

[7] T. Hensgens, T. Fujita, L. Janssen, X. Li, C. J. Van Diepen, C. Reichl, W. Wegscheider, S. Das Sarma, and L. M. K. Vandersypen, *Quantum simulation of a Fermi-Hubbard model using a semiconductor quantum dot array*, Nature (London) **548**, 70 (2017).

[8] A. Singha, M. Gibertini, B. Karmakar, S. Yuan, M. Polini, G. Vignale, M. I. Katsnelson, A. Pinczuk, L. N. Pfeiffer, K. W. West, and V. Pellegrini, *Two-dimensional Mott-Hubbard electrons in an artificial honeycomb lattice*, Science **332**, 1176 (2011).

[9] J. Salfi, J. A. Mol, R. Rahman, G. Klimeck, M. Y. Simmons, L. C. L. Hollenberg, and S. Rogge, *Quantum simulation of the Hubbard model with dopant atoms in silicon*, Nat. Commun. **7**, 11342 (2016).

[10] J. P. Dehollain, U. Mukhopadhyay, V. P. Michal, Y. Wang, B. Wunsch, C. Reichl, W. Wegscheider, M. S. Rudner, E. Demler, and L. M. K. Vandersypen, *Nagaoka ferromagnetism observed in a quantum dot plaquette*, Nature (London) **579**, 528 (2020).

[11] C. J. van Diepen, T. K. Hsiao, U. Mukhopadhyay, C. Reichl, W. Wegscheider, and L. M. K. Vandersypen, *Quantum simulation of antiferromagnetic Heisenberg chain with gate-defined quantum dots*, Phys. Rev. X **11**, 041025 (2021).

[12] C.-A. Wang, C. Déprez, H. Tidjani, W. I. L. Lawrie, N. W. Hendrickx, A. Sammak, G. Scappucci, and M. Veldhorst, *Probing resonating valence bonds on a programmable germanium quantum simulator*, npj Quantum Inf. **9**, 58 (2023).

[13] M. Kiczynski, S. K. Gorman, H. Geng, M. B. Donnelly, Y. Chung, Y. He, J. G. Keizer, and M. Y. Simmons, *Engineering topological states in atom-based semiconductor quantum dots*, Nature (London) **606**, 694 (2022).

[14] E. Abrahams, S. V. Kravchenko, and M. P. Sarachik, *Metallic behavior and related phenomena in two dimensions*, Rev. Mod. Phys. **73**, 251 (2001).

[15] Y. Zhou, J. Sung, E. Brutschea, I. Esterlis, Y. Wang, G. Scuri, R. J. Gelly, H. Heo, T. Taniguchi, K. Watanabe, G. Zaránd, M. D. Lukin, P. Kim, E. Demler, and H. Park, *Bilayer Wigner crystals in a transition metal dichalcogenide heterostructure*, Nature (London) **595**, 48 (2021).

[16] Y. Xu, S. Liu, D. A. Rhodes, K. Watanabe, T. Taniguchi, J. Hone, V. Elser, K. F. Mak, and J. Shan, *Correlated insulating states at fractional fillings of moiré superlattices*, Nature (London) **587**, 214 (2020).

[17] H. Li, S. Li, E. C. Regan, D. Wang, W. Zhao, S. Kahn, K. Yumigeta, M. Blei, T. Taniguchi, K. Watanabe, S. Tongay, A. Zettl, M. F. Crommie, and F. Wang, *Imaging two-dimensional generalized Wigner crystals*, Nature (London) **597**, 650 (2021).

[18] D. F. Agterberg, J. C. S. Davis, S. D. Edkins, E. Fradkin, D. J. Van Harlingen, S. A. Kivelson, P. A. Lee, L. Radzihovsky, J. M. Tranquada, and Y. Wang, *The physics of pair-density waves: Cuprate superconductors and beyond*, Annu. Rev. Condens. Matter Phys. **11**, 231 (2020).

[19] J. Frenkel, *On the transformation of light into heat in solids. I*, Phys. Rev. **37**, 17 (1931).

[20] D. Jérome, T. M. Rice, and W. Kohn, *Excitonic insulator*, Phys. Rev. **158**, 462 (1967).

[21] W. Kohn and D. Sherrington, *Two kinds of bosons and Bose condensates*, Rev. Mod. Phys. **42**, 1 (1970).

[22] K. Slagle and L. Fu, *Charge transfer excitations, pair density waves, and superconductivity in moiré materials*, Phys. Rev. B **102**, 235423 (2020).

[23] V. Crépel and L. Fu, *New mechanism and exact theory of superconductivity from strong repulsive interaction*, Sci. Adv. **7**, eabh2233 (2023).

[24] E. Guardado-Sanchez, B. M. Spar, P. Schauss, R. Belyansky, J. T. Young, P. Bienias, A. V. Gorshkov, T. Iadecola, and W. S. Bakr, *Quench dynamics of a Fermi gas with strong nonlocal interactions*, Phys. Rev. X **11**, 021036 (2021).

[25] L. Su, A. Douglas, M. Szurek, R. Groth, S. F. Ozturk, A. Krahn, A. H. Hébert, G. A. Phelps, S. Ebadi, S. Dickerson, F. Ferlaino, O. Marković, and M. Greiner, *Dipolar quantum solids emerging in a Hubbard quantum simulator*, Nature (London) **622**, 724 (2023).

[26] I. Bloch, J. Dalibard, and W. Zwerger, *Many-body physics with ultracold gases*, Rev. Mod. Phys. **80**, 885 (2008).

[27] J. Argüello-Luengo, A. González-Tudela, T. Shi, P. Zoller, and J. I. Cirac, *Analogue quantum chemistry simulation*, Nature (London) **574**, 215 (2019).

[28] A. M. Kaufman and K.-K. Ni, *Quantum science with optical tweezer arrays of ultracold atoms and molecules*, Nat. Phys. **17**, 1324 (2021).

[29] L. Chomaz, I. Ferrier-Barbut, F. Ferlaino, B. Laburthe-Tolra, B. L. Lev, and T. Pfau, *Dipolar physics: A review of experiments with magnetic quantum gases*, Rep. Prog. Phys. **86**, 026401 (2023).

[30] B. Yan, S. A. Moses, B. Gadway, J. P. Covey, K. R. A. Hazzard, A. M. Rey, D. S. Jin, and J. Ye, *Observation of dipolar spin-exchange interactions with lattice-confined polar molecules*, Nature (London) **501**, 521 (2013).

[31] H. Bernien, S. Schwartz, A. Keesling, H. Levine, A. Omran, H. Pichler, S. Choi, A. S. Zibrov, M. Endres, M. Greiner, V. Vuletić, and M. D. Lukin, *Probing many-body dynamics on a 51-atom quantum simulator*, Nature (London) **551**, 579 (2017).

[32] G. Semeghini, H. Levine, A. Keesling, S. Ebadi, T. T. Wang, D. Bluvstein, R. Verresen, H. Pichler, M. Kalinowski, R. Samajdar, A. Omran, S. Sachdev, A. Vishwanath, M. Greiner, V. Vuletić, and M. D. Lukin, *Probing topological spin liquids on a programmable quantum simulator*, Science **374**, 1242 (2021).

[33] D. Nandi, A. D. K. Finck, J. P. Eisenstein, L. N. Pfeiffer, and K. W. West, *Exciton condensation and perfect Coulomb drag*, Nature (London) **488**, 481 (2012).

[34] T. J. Gramila, J. P. Eisenstein, A. H. MacDonald, L. N. Pfeiffer, and K. W. West, *Mutual friction between parallel two-dimensional electron systems*, Phys. Rev. Lett. **66**, 1216 (1991).

[35] M. Yamamoto, M. Stopa, Y. Tokura, Y. Hirayama, and S. Tarucha, *Negative Coulomb drag in a one-dimensional wire*, Science **313**, 204 (2006).

[36] B. N. Narozhny and A. Levchenko, *Coulomb drag*, Rev. Mod. Phys. **88**, 025003 (2016).

[37] M. Kellogg, I. B. Spielman, J. P. Eisenstein, L. N. Pfeiffer, and K. W. West, *Observation of quantized Hall drag in a strongly correlated bilayer electron system*, Phys. Rev. Lett. **88**, 126804 (2002).

[38] E. Tutuc, M. Shayegan, and D. A. Huse, *Counterflow measurements in strongly correlated GaAs hole bilayers: Evidence for electron-hole pairing*, Phys. Rev. Lett. **93**, 036802 (2004).

[39] D. Laroche, G. Gervais, M. P. Lilly, and J. L. Reno, *Positive and negative Coulomb drag in vertically integrated one-dimensional quantum wires*, Nat. Nanotechnol. **6**, 793 (2011).

[40] R. V. Gorbachev, A. K. Geim, M. I. Katsnelson, K. S. Novoselov, T. Tudorovskiy, I. V. Grigorieva, A. H. MacDonald, S. V. Morozov, K. Watanabe, T. Taniguchi, and L. A. Ponomarenko, *Strong Coulomb drag and broken symmetry in double-layer graphene*, Nat. Phys. **8**, 896 (2012).

[41] J. I. A. Li, T. Taniguchi, K. Watanabe, J. Hone, and C. R. Dean, *Excitonic superfluid phase in double bilayer graphene*, Nat. Phys. **13**, 751 (2017).

[42] X. Liu, K. Watanabe, T. Taniguchi, B. I. Halperin, and P. Kim, *Quantum Hall drag of exciton condensate in graphene*, Nat. Phys. **13**, 746 (2017).

[43] B. Pandey, G. Alvarez, and E. Dagotto, *Excitonic wave-packet evolution in a two-orbital Hubbard model chain: A real-time real-space study*, Phys. Rev. B **104**, L220302 (2021).

[44] T. Kaneko, K. Seki, and Y. Ohta, *Excitonic insulator state in the two-orbital Hubbard model: Variational cluster approach*, Phys. Rev. B **85**, 165135 (2012).

[45] D. Vu and S. D. Sarma, *Excitonic phases in a spatially separated electron-hole ladder model*, Phys. Rev. B **108**, 235158 (2023).

[46] D. V. Averin, A. N. Korotkov, and Y. V. Nazarov, *Transport of electron-hole pairs in arrays of small tunnel junctions*, Phys. Rev. Lett. **66**, 2818 (1991).

[47] M. Matters, J. J. Versluys, and J. E. Mooij, *Electron-hole transport in capacitively coupled 1D arrays of small tunnel junctions*, Phys. Rev. Lett. **78**, 2469 (1997).

[48] H. Shimada and P. Delsing, *Current mirror effect and correlated Cooper-pair transport in coupled arrays of small Josephson junctions*, Phys. Rev. Lett. **85**, 3253 (2000).

[49] G. Shinkai, T. Hayashi, T. Ota, K. Muraki, and T. Fujisawa, *Bidirectional current drag induced by two-electron cotunneling in coupled double quantum dots*, Appl. Phys. Express **2**, 081101 (2009).

[50] D. M. Zajac, T. M. Hazard, X. Mi, E. Nielsen, and J. R. Petta, *Scalable gate architecture for a one-dimensional array of semiconductor spin qubits*, Phys. Rev. Appl. **6**, 054013 (2016).

[51] S. G. J. Philips, M. T. Mądzik, S. V. Amitonov, S. L. de Snoo, M. Russ, N. Kalhor, C. Volk, W. I. L. Lawrie, D. Brousse, L. Tryputen, B. P. Wuetz, A. Sammak, M. Veldhorst, G. Scappucci, and L. M. K. Vandersypen, *Universal control of a six-qubit quantum processor in silicon*, Nature (London) **609**, 919 (2022).

[52] W. Ha, S. D. Ha, M. D. Choi, Y. Tang, A. E. Schmitz, M. P. Levendorf, K. Lee, J. M. Chappell, T. S. Adams, D. R. Hulbert, E. Acuna, R. S. Noah, J. W. Matten, M. P. Jura, J. A. Wright, M. T. Rakher, and M. G. Borselli, *A flexible design platform for* Si/SiGe *exchange-only qubits with low disorder*, Nano Lett. **22**, 1443 (2022).

[53] P.-A. Mortemousque, B. Jadot, E. Chanrion, V. Thiney, C. Bäuerle, A. Ludwig, A. D. Wieck, M. Urdampilleta, and T. Meunier, *Enhanced spin coherence while displacing electron in a two-dimensional array of quantum dots*, PRX Quantum **2**, 030331 (2021).

[54] E. Chanrion, D. J. Niegemann, B. Bertrand, C. Spence, B. Jadot, J. Li, P.-A. Mortemousque, L. Hutin, R. Maurand, X. Jehl, M. Sanquer, S. De Franceschi, C. Bäuerle, F. Balestro, Y.-M. Niquet, M. Vinet, T. Meunier, and M. Urdampilleta, *Charge detection in an array of CMOS quantum dots*, Phys. Rev. Appl. **14**, 024066 (2020).

[55] F. K. Unseld, M. Meyer, M. T. Mądzik, F. Borsoi, S. L. de Snoo, S. V. Amitonov, A. Sammak, G. Scappucci, M. Veldhorst, and L. M. K. Vandersypen, *A 2D quantum dot array in planar* $^{28}$Si/SiGe, Appl. Phys. Lett. **123**, 084002 (2023).

[56] N. W. Hendrickx, W. I. L. Lawrie, M. Russ, F. van Riggelen, S. L. de Snoo, R. N. Schouten, A. Sammak, G. Scappucci, and M. Veldhorst, *A four-qubit germanium quantum processor*, Nature (London) **591**, 580 (2021).

[57] M. Lodari, A. Tosato, D. Sabbagh, M. A. Schubert, G. Capellini, A. Sammak, M. Veldhorst, and G. Scappucci, *Light effective hole mass in undoped* Ge/SiGe *quantum wells*, Phys. Rev. B **100**, 041304(R) (2019).

[58] G. Scappucci, C. Kloeffel, F. A. Zwanenburg, D. Loss, M. Myronov, J. J. Zhang, S. De Franceschi, G. Katsaros, and M. Veldhorst, *The germanium quantum information route*, Nat. Rev. Mater. **6**, 926 (2021).

[59] F. Borsoi, N. W. Hendrickx, V. John, M. Meyer, S. Motz, F. van Riggelen, A. Sammak, S. L. de Snoo, G. Scappucci, and M. Veldhorst, *Shared control of a 16 semiconductor quantum dot crossbar array*, Nat. Nanotechnol. **19**, 21 (2023).

[60] M. Lodari, N. W. Hendrickx, W. I. L. Lawrie, T.-K. Hsiao, L. M. K. Vandersypen, A. Sammak, M. Veldhorst, and G. Scappucci, *Low percolation density and charge noise with holes in germanium*, Mat. Quantum Technol. **1**, 011002 (2021).

[61] C. J. van Diepen, P. T. Eendebak, B. T. Buijtendorp, U. Mukhopadhyay, T. Fujita, C. Reichl, W. Wegscheider, and L. M. K. Vandersypen, *Automated tuning of inter-dot tunnel coupling in double quantum dots*, Appl. Phys. Lett. **113**, 33101 (2018).

[62] T.-K. Hsiao, C. J. van Diepen, U. Mukhopadhyay, C. Reichl, W. Wegscheider, and L. M. K. Vandersypen, *Efficient orthogonal control of tunnel couplings in a quantum dot array*, Phys. Rev. Appl. **13**, 054018 (2020).

[63] H. Qiao, Y. P. Kandel, K. Deng, S. Fallahi, G. C. Gardner, M. J. Manfra, E. Barnes, and J. M. Nichol, *Coherent multispin exchange coupling in a quantum-dot spin chain*, Phys. Rev. X **10**, 031006 (2020).

[64] F. R. Braakman, P. Barthelemy, C. Reichl, W. Wegscheider, and L. M. K. Vandersypen, *Long-distance coherent coupling in a quantum dot array*, Nat. Nanotechnol. **8**, 432 (2013).

[65] T. H. Oosterkamp, T. Fujisawa, W. G. Van Der Wiel, K. Ishibashi, R. V. Hijman, S. Tarucha, and L. P. Kouwenhoven, *Microwave spectroscopy of a quantum-dot molecule*, Nature (London) **395**, 873 (1998).

[66] We note that although $t_{15}$ is higher than other interchannel tunnel couplings, since electron-hole pair transport is a cotunneling process and since $t_{26}$ remains below 1 μeV, the correlated hopping of an electron-hole pair across the channels is still 3 orders of magnitude smaller than the hopping along the channel direction.

[67] In the experiment, we apply a global virtual gate voltage on the bottom channel and convert the global voltage to a global energy offset using an averaged bottom-channel lever arm 112 μeV/mV.

[68] Strictly speaking, exciton condensation does not occur in 1D or 2D at finite temperature. However, for real experimental systems we can have quasicondensation when the correlation length exceeds the system size [88].

[69] M. Sigrist, Thomas Ihn, K. Ensslin, M. Reinwald, and W. Wegscheider, *Coherent probing of excited quantum dot states in an interferometer*, Phys. Rev. Lett. **98**, 036805 (2007).

[70] S. Gustavsson, R. Leturcq, M. Studer, T. Ihn, K. Ensslin, D. C. Driscoll, and A. C. Gossard, *Time-resolved detection of single-electron interference*, Nano Lett. **8**, 2547 (2008).

[71] G. Shinkai, T. Hayashi, T. Ota, and T. Fujisawa, *Correlated coherent oscillations in coupled semiconductor charge qubits*, Phys. Rev. Lett. **103**, 056802 (2009).

[72] H.-O. Li, G. Cao, G.-D. Yu, M. Xiao, G.-C. Guo, H.-W. Jiang, and G.-P. Guo, *Controlled quantum operations of a semiconductor three-qubit system*, Phys. Rev. Appl. **9**, 024015 (2018).

[73] K. D. Petersson, J. R. Petta, H. Lu, and A. C. Gossard, *Quantum coherence in a one-electron semiconductor charge qubit*, Phys. Rev. Lett. **105**, 246804 (2010).

[74] X. Zhang, E. Morozova, M. Rimbach-Russ, D. Jirovec, T.-K. Hsiao, P. C. Fariña, C.-A. Wang, S. D. Oosterhout, A. Sammak, G. Scappucci, M. Veldhorst, and L. M. K. Vandersypen, *Universal control of four singlet-triplet qubits*, arXiv:2312.16101.

[75] Holes in strained germanium have spin-3/2, but the large heavy-hole light-hole splitting leads to an effective two-level system.
[76] C. N. Yang and S. C. Zhang, $SO_4$ *symmetry in a Hubbard model*, Mod. Phys. Lett. B **04**, 759 (1990).
[77] M. Rizzi, D. Rossini, G. De Chiara, S. Montangero, and R. Fazio, *Phase diagram of spin-1 bosons on one-dimensional lattices*, Phys. Rev. Lett. **95**, 240404 (2005).
[78] G. V. Shlyapnikov and A. M. Tsvelik, *Polar phase of one-dimensional bosons with large spin*, New J. Phys. **13**, 065012 (2011).
[79] R. Winkler, *Spin-Orbit Coupling Effects in Two-Dimensional Electron and Hole Systems* (Springer Berlin, Heidelberg, 2003), 10.1007/b13586.
[80] L. P. Gor'kov and E. I. Rashba, *Superconducting 2D system with lifted spin degeneracy: Mixed singlet-triplet state*, Phys. Rev. Lett. **87**, 037004 (2001).
[81] V. N. Golovach, A. Khaetskii, and D. Loss, *Spin relaxation at the singlet-triplet crossing in a quantum dot*, Phys. Rev. B **77**, 045328 (2008).
[82] C. Comte and P. Nozières, *Exciton Bose condensation: The ground state of an electron-hole gas—I. Mean field description of a simplified model*, J. Phys. (Paris) **43**, 1069 (1982).
[83] G. A. Fiete, *Colloquium: The spin-incoherent Luttinger liquid*, Rev. Mod. Phys. **79**, 801 (2007).
[84] T.-K. Hsiao *et al.*, *Data for 'Exciton transport in a germanium quantum dot ladder' by Tzu-Kan Hsiao et al.*, Zenodo (2023), 10.5281/zenodo.8105397.
[85] L. D. Landau, *Zur theorie der energieübertragung. II*, Phys. Soviet Union **2**, 46 (1932).
[86] C. Zener, *Non-adiabatic crossing of energy levels*, Proc. R. Soc. A **137**, 696 (1932).
[87] J. Knörzer, C. J. van Diepen, T.-K. Hsiao, G. Giedke, U. Mukhopadhyay, C. Reichl, W. Wegscheider, J. I. Cirac, and L. M. K. Vandersypen, *Long-range electron-electron interactions in quantum dot systems and applications in quantum chemistry*, Phys. Rev. Res. **4**, 033043 (2022).
[88] D. S. Petrov, G. V. Shlyapnikov, and J. T. M. Walraven, *Regimes of quantum degeneracy in trapped 1D gases*, Phys. Rev. Lett. **85**, 3745 (2000).